

**Key Points:**

- A carbon dioxide infrared emission at 4.26 microns associated with the aurora is observed by the Atmospheric Infrared Sounder (AIRS) instrument
- A new non-local thermodynamic equilibrium index provides a quantitative measure of the carbon dioxide auroral-associated emission
- The AIRS auroral observations are confirmed by simultaneous Sounding of the Atmosphere using Broadband Emission Radiometry measurements and the SuperMAG Electrojet index

**Correspondence to:**

K. Bossert,  
katrina.bossert@asu.edu

**Citation:**

Bossert, K., Hoffmann, L., Mlynczak, M., & Hunt, L. (2023). Observations of 4.26  $\mu\text{m}$  CO<sub>2</sub> auroral emissions from AIRS nadir sounder measurements. *Geophysical Research Letters*, 50, e2023GL103856. <https://doi.org/10.1029/2023GL103856>

Received 24 MAR 2023  
Accepted 25 MAY 2023

## Observations of 4.26 $\mu\text{m}$ CO<sub>2</sub> Auroral Emissions From AIRS Nadir Sounder Measurements

Katrina Bossert<sup>1,2</sup> , Lars Hoffmann<sup>3</sup> , Martin Mlynczak<sup>4</sup> , and Linda Hunt<sup>5</sup>

<sup>1</sup>School of Earth and Space Exploration, Arizona State University, Tempe, AZ, USA, <sup>2</sup>School of Mathematical and Statistical Sciences, Arizona State University, Tempe, AZ, USA, <sup>3</sup>Jülich Supercomputing Centre, Forschungszentrum Jülich, Jülich, Germany, <sup>4</sup>NASA Langley Research Center, Hampton, VA, USA, <sup>5</sup>Science Systems and Applications, Inc., Hampton, VA, USA

**Abstract** The Atmospheric Infrared Sounder (AIRS) instrument onboard the NASA Aqua satellite is used to observe aurora associated with the CO<sub>2</sub> 4.26  $\mu\text{m}$  emission. These observations are due to non-local thermodynamic equilibrium (NLTE) resulting from the vibrational excitation of CO<sub>2</sub>, which arises in the process of auroral energetic particle precipitation, as opposed to the dayside NLTE occurring due to solar radiation. The observations are confirmed to be associated with aurora using the Sounding of the Atmosphere using Broadband Emission Radiometry (SABER) limb measurements and the SuperMAG Electrojet (SME) index. The high spectral resolution and low noise associated with the AIRS instrument allows for the emission spectrum to be calculated and confirmed to arise from CO<sub>2</sub>. Our new NLTE index values derived from AIRS provide the ability to globally measure auroral events associated with CO<sub>2</sub> with a spatial resolution on the order of  $\sim$ 13.5 km.

**Plain Language Summary** The aurora are caused by energetic particle precipitation into Earth's atmosphere due to energy buildup and release in Earth's magnetic field from interaction with the solar wind. These energetic particles smash into Earth's atmosphere with high energy, and react with atoms and molecules in the atmosphere. There are many types of emissions of light that are associated with Earth's aurora. One of these emissions is the infrared emission centered near 4.26  $\mu\text{m}$  associated with excited CO<sub>2</sub> molecules. When CO<sub>2</sub> is vibrationally excited through an exchange of energy with an N<sub>2</sub> molecule excited by auroral particles, the CO<sub>2</sub> molecule eventually relaxes from this state and releases a photon near 4.26  $\mu\text{m}$ . This research presents a satellite observation from NASA's AIRS instrument allowing for the CO<sub>2</sub> auroral emission to be viewed and mapped from space.

### 1. Introduction

The Atmospheric Infrared Sounder (AIRS) instrument onboard the NASA Aqua satellite was launched in 2002 and has been used to study the temperature in the stratosphere using CO<sub>2</sub> emissions at 4.26 and 15  $\mu\text{m}$  (Hoffmann & Alexander, 2009). While both of these emissions can be used to study temperatures during thermodynamic equilibrium, the 4.26  $\mu\text{m}$  emission specifically is more sensitive non-local thermodynamic equilibrium (NLTE) during the daytime (DeSouza-Machado et al., 2007). For a nadir sounder such as AIRS, the 4.3  $\mu\text{m}$  NLTE effect can be measured, while the 15  $\mu\text{m}$  NLTE effect is too small to be observed. Additionally, the 4.26  $\mu\text{m}$  emission itself is susceptible to enhancements due to energetic particle precipitation during geomagnetic disturbances. This emission enhancement is known for both NO<sup>+</sup> (Mertens, Fernandez, et al., 2008; Mertens, Winick, et al., 2008; O'Neil et al., 2007) and CO<sub>2</sub> (Kalogerakis et al., 2016; Kumer, 1977; Sharma et al., 2015; Winick et al., 1987). The CO<sub>2</sub> auroral excitation results in NLTE, and has previously been discussed with regards to the Cross-track Infrared Sounder (CrIS) NLTE observations in comparison to modeled NLTE radiances, which do not capture the full contribution to NLTE due to aurora (Z. Li et al., 2020), as models have assumed NLTE conditions that occur during the daytime. Additionally, broadband IR measurements from VIIRS have also detected auroral emissions (Seaman & Miller, 2013), and the range of observed infrared wavelengths includes the NO<sup>+</sup> and CO<sub>2</sub> emissions.

Energetic particle precipitation changes the thermal energy balance in the mesosphere, thermosphere, and ionosphere. It results in significant chemical reactions, making energetic particle precipitation of interest for understanding both the chemistry and thermodynamics in this region of the atmosphere. Satellite and ground-based imaging of specific emission lines associated with aurora have been used to calculate auroral input energy

© 2023. The Authors.

This is an open access article under the terms of the [Creative Commons Attribution License](#), which permits use, distribution and reproduction in any medium, provided the original work is properly cited.

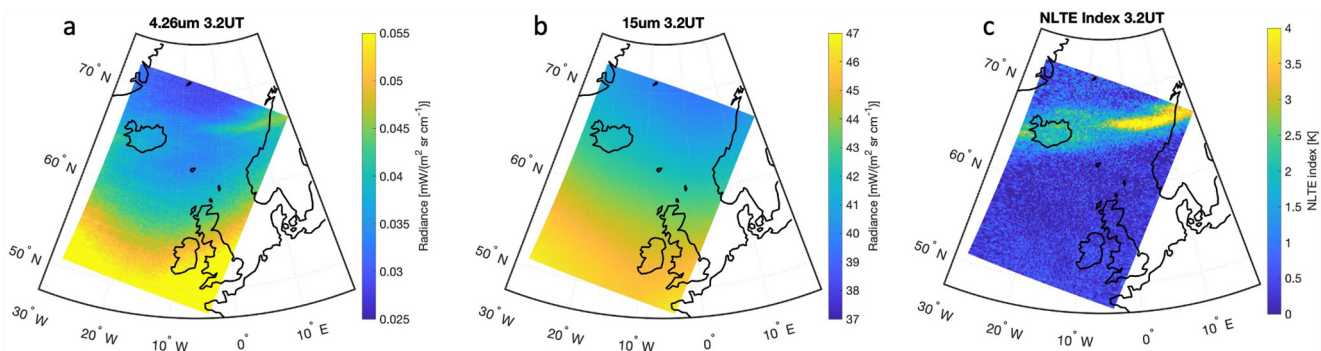


**Figure 1.** An example Atmospheric Infrared Sounder granule is used at  $\sim 3.2$  UT on 14 October 2016 to demonstrate average spectral radiances associated with aurora. Plot (a) shows spectral radiances averaged over 75 channels from 2,310 to 2,380  $\text{cm}^{-1}$  covering the 4.26  $\mu\text{m}$  emission. Plot (b) shows spectral radiances averaged over 120 channels from 650 to 680  $\text{cm}^{-1}$  covering the 15  $\mu\text{m}$  waveband. Plot (c) shows the calculated non-local thermodynamic equilibrium index.

to energetic particle precipitation (Gabrielse et al., 2021; Hecht et al., 1989, 2006; J. Li et al., 2022; Sotirelis et al., 2013; Strickland et al., 1989). Energetic particle precipitation from aurora and solar activity has also been associated with increased NO<sub>x</sub> (López-Puertas et al., 2005; Randall et al., 2007). The necessity of understanding the full spectrum of energetic electrons for adequately characterizing the chemistry in the middle atmosphere has also previously been discussed (Randall et al., 2015). Additionally, understanding energetic input due to aurora and particle precipitation is important for linking to atmospheric dynamics such as the generation of traveling ionospheric disturbances due to joule heating (Sheng et al., 2020).

Observations presented here demonstrate an AIRS 4.26  $\mu\text{m}$  emission associated with auroral precipitation. The observations are compared with Sounding of the Atmosphere using Broadband Emission Radiometry (SABER) observations and the SME. These AIRS measurements provide a unique means of observing auroral emissions at 4.26  $\mu\text{m}$  spatially with a nadir viewing instrument. The emission spectra from the nadir measurements in this spectral range were found to be largely due to CO<sub>2</sub>. To isolate emissions due to 4.26  $\mu\text{m}$ , a new NLTE index, discussed in the following sections, is calculated. The results provide a map of CO<sub>2</sub> emissions during nighttime conditions due to energetic particle precipitation from aurora.

## 2. Data and Methods

### 2.1. The AIRS Instrument and a Measurement Derived NLTE Index

In this study, we initially identified the presence of NLTE effects in the AIRS observations by visual inspection of radiance measurements covering the 4.26 and 15  $\mu\text{m}$  carbon dioxide (CO<sub>2</sub>) fundamental bands. As an example, Figure 1 shows spectral mean radiances of granule 32 of AIRS measurements on 14 October 2016, measured from 3:12 to 3:18 UTC using a set of 75 channels from 2,310 to 2,380  $\text{cm}^{-1}$  covering the 4.26  $\mu\text{m}$  waveband and a set of 120 channels from 650 to 680  $\text{cm}^{-1}$  covering the 15  $\mu\text{m}$  waveband. Here, the radiance measurements of the two channel set have been averaged to reduce the measurement noise and to make some weaker NLTE features visible. A visual inspection of the AIRS nighttime measurements shows locally increased radiances due to NLTE in the 4.26  $\mu\text{m}$  waveband (Figure 1a), which are absent in the 15  $\mu\text{m}$  waveband (Figure 1b). The increased 4.26  $\mu\text{m}$  radiances are found in a belt extending from Iceland to Scandinavia from 65 to 70°N. The belt of increased radiances is co-located with the Aurora Borealis and attributed to excitation of the CO<sub>2</sub> molecules to NLTE conditions, which will be shown and further discussed in following sections.

In order to quantify the strength of the NLTE signals in the AIRS measurements, we defined a NLTE index (NI) using the 4.26 and 15 micron radiance measurements. Such an NI can be defined in various ways. In principle, it could be defined as simple as taking a brightness temperature difference of the 4.26 and 15  $\mu\text{m}$  radiance measurements of each satellite footprint. However, we found this approach did not work well because the 4.26 and 15  $\mu\text{m}$  AIRS channel sets considered here have different spectral mean vertical coverage and sensitivity due to the different temperature weighting functions, which would map into the calculation of the NI. Next to spectral differencing for defining the NI, another option would be spatial differencing of radiance measurements using separate footprints located inside or outside regions being affected by NLTE. However, spatial differencing

requires various choices and parameter tests of the method, for example, with respect to proper smoothing and removal of the background-state. For these reasons, we developed a more sophisticated approach to define and calculate an NI from the AIRS measurements.

We calculate the NI from the AIRS measurements in a two-step procedure. In the first step, we conduct a full non-linear stratospheric temperature retrieval using the AIRS measurements in the 15  $\mu\text{m}$  waveband. The retrieval scheme applied here is essentially the same as the retrieval scheme described by Hoffmann and Alexander (2009). The retrieval provides stratospheric temperatures in the height range of about 20–55 km with a vertical resolution of 7–11 km and retrieval noise of about 1.5–2 K in the same range. While the retrieval applies a radiative transfer model that is not capable of simulating NLTE effects, the retrieved temperature profile  $\hat{T}_{\text{LTE}}(z, 15 \mu\text{m})$  is not affected by this, because the 15  $\mu\text{m}$  channels applied in the scheme are not affected by NLTE (DeSouza-Machado et al., 2007). In the second step, we apply the radiative transfer model and the temperature profile retrieved from the 15  $\mu\text{m}$  radiance measurements to simulate the 4.26  $\mu\text{m}$  radiance measurements AIRS would make under LTE conditions. Finally, the NI is calculated as the difference between the real AIRS spectral mean brightness temperature measurements including the NLTE effects and the simulated brightness temperature measurements assuming LTE conditions,

$$\text{NI} = \overline{\text{BT}}_{\text{meas}}(4.26 \mu\text{m}, T_{\text{non-LTE}}(z)) - \overline{\text{BT}}_{\text{sim}}(4.26 \mu\text{m}, \hat{T}_{\text{LTE}}(z, 15 \mu\text{m})) \quad (1)$$

As an example, Figure 1c shows the NI calculated from the AIRS measurements for the case study discussed earlier. As NLTE conditions yield increased molecular excitation and increased radiance emitted by the CO<sub>2</sub> molecules, the NI increases in the presence of NLTE conditions. From the example shown here, the maximum NI is about 4 K whereas the measurement noise is about 0.5 K. We note that while the NI is usually well-defined, in the case of extreme temperature fluctuations, for example, due to the presence of large-amplitude mountain waves, the index may misdetect these fluctuations as NLTE signals. This issue arises from remaining, small differences in terms of vertical coverage and sensitivity of the AIRS 4.26 and 15  $\mu\text{m}$  channels selected for this analysis. However, based on the inspection of a larger number of cases of AIRS NLTE observations, we conclude that this issue is generally not severe, but should be kept in mind when analyzing individual cases. Such cases can be identified using gravity wave detection methods for AIRS observations as described by Hoffmann et al. (2013, 2014).

## 2.2. Comparison of AIRS NLTE Index and SME Data

The NLTE index was calculated over the northern polar region for a time period of increased auroral activity. The time period extends from 7.5 UT on 13 October 2016 to 6.5 UT on 14 October 2016 and uses 15 granules. The resulting NLTE index signals in Figure 2a clearly show the shape of the aurora. AIRS nightside granules were used (solar zenith angles were between 100 and 130° for data shown), and these times approximately spanned just before magnetic midnight to a few hours before magnetic midnight, which generally overlaps times of expected auroral activity on the night side (Laundal & Richmond, 2016). While not shown here, similar emissions can be observed in the southern hemisphere during nighttime conditions. The SuperMAG Electrojet (SME) index (Gjerloev, 2012; Newell & Gjerloev, 2011a, 2011b) is associated with global auroral power. The SME uses over 100 magnetometer sites as opposed to the 12 used in the auroral electrojet (AE) index calculation, and has previously demonstrated a strong correlation with total nightside auroral power. The SME is used here to demonstrate times of increased auroral activity. The SME is plotted during an overlapped time range in Figure 2b. As can be observed from the plots in Figure 2, the times of stronger NLTE index signals correspond to times of stronger SME index. This comparison provides a means of demonstrating the auroral influence on AIRS NLTE index calculations. Figure 2a also shows how this data product can be used to give a global snapshot of hemispheric auroral activity over a 24 hr period.

## 2.3. Comparison With SABER Coincident Measurements

The AIRS NLTE index observations were further compared to coincident SABER measurements to verify the presence of auroral emissions. Figure 3a shows an AIRS granule 15 (1:30–1:36UT) with calculated NLTE index values on 14 October 2016. Figures 3b–3d show coincident SABER spectrally integrated radiance measurements of CO<sub>2</sub> 15.2  $\mu\text{m}$ , CO<sub>2</sub> 4.26  $\mu\text{m}$ , and O<sub>2</sub> 1.28  $\mu\text{m}$  volume emission rate during this time. Figure 3e shows AIRS

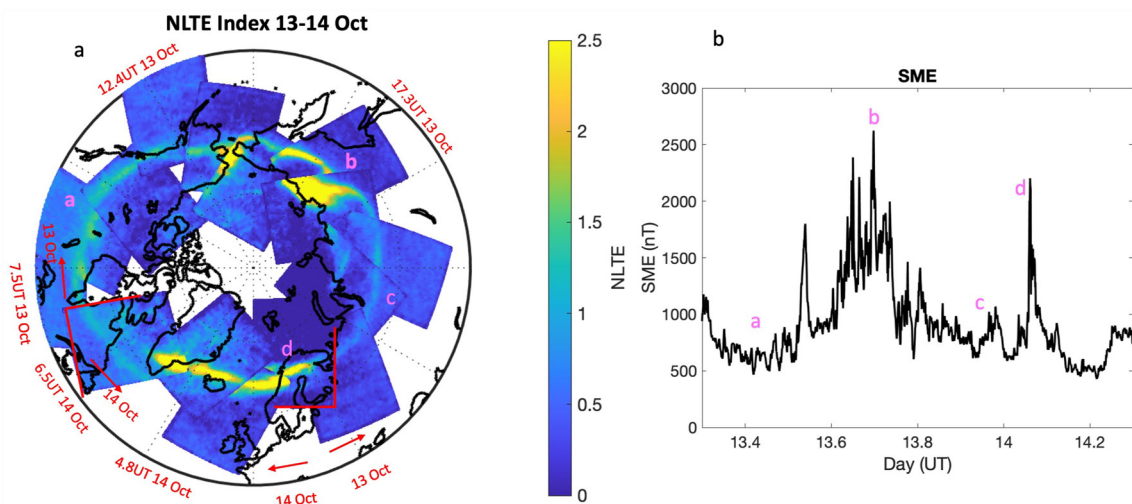


**Figure 2.** Plot (a) shows the Atmospheric Infrared Sounder non-local thermodynamic equilibrium (NLTE) Index calculated for 15 granules over a 24 hr period of increased auroral activity. Plot (b) shows the SuperMAG Electrojet (SME) index for the same time period demonstrating that times of increased SME correspond to increased NLTE Index.

granule 32 (3:12–3:18 UT) and corresponding NLTE index signals on 14 October 2016. Corresponding SABER measurements are shown in Figures 3f–3h. In both cases, SABER demonstrates there is no enhancement in 15.2  $\mu\text{m}$  overlapping the regions closest to the largest AIRS NLTE index calculation. SABER has previously been used to demonstrate an auroral enhancement in the 4.26  $\mu\text{m}$  channel due to  $\text{CO}_2$  (Winick et al., 2004), and at higher altitudes due to  $\text{NO}^+$  (Mertens et al., 2008a, 2008b). Enhancements in the SABER 4.26  $\mu\text{m}$  channel are observed for these AIRS overlap examples, especially for the limb views that most closely overlap the aurora (red dots in Figures 3a and 3e, and red lines in Figures 3c and 3g). SABER has also been used to study auroral emissions associated with  $\text{O}_2$  airglow at 1.28  $\mu\text{m}$  (Gao et al., 2020). For these cases, enhancements are observed in the 1.28  $\mu\text{m}$  channel from  $\sim$ 100 to 120 km. It is noted here that SABER measurements are limb measurements, so have more sensitivity to emissions at higher altitudes associated with  $\text{NO}^+$  (Mertens, Winick, et al., 2008), that

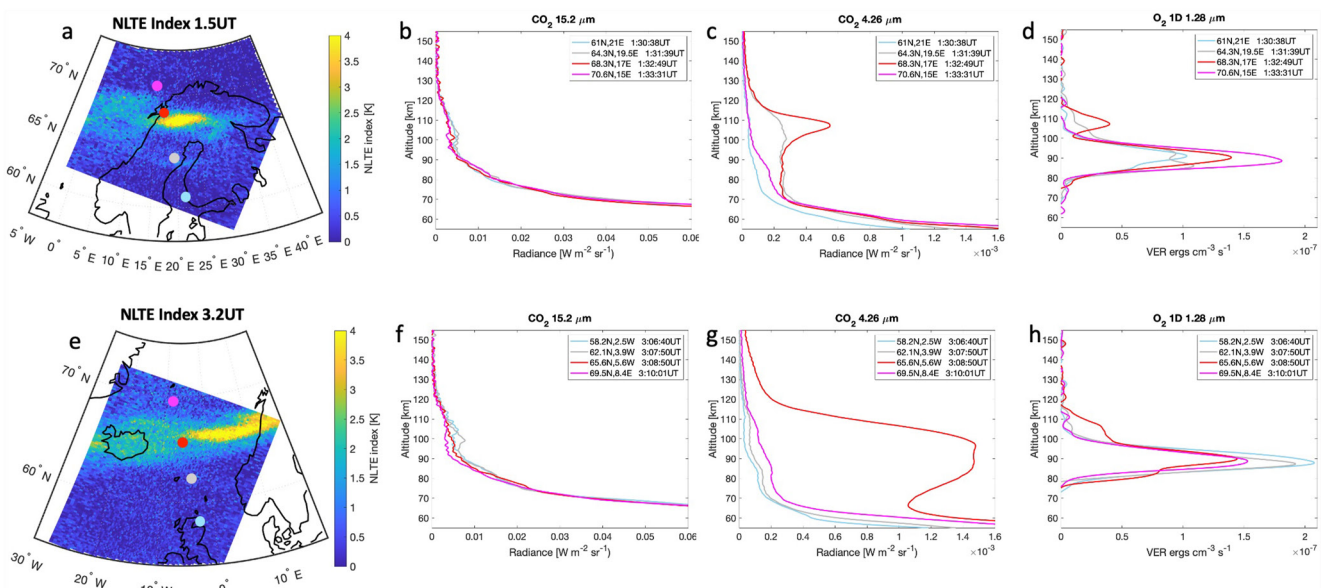


**Figure 3.** Plot (a) shows the Atmospheric Infrared Sounder (AIRS) non-local thermodynamic equilibrium index on 14 October 2016 at 1.5 UT. Plots (b–d) show corresponding Sounding of the Atmosphere using Broadband Emission Radiometry (SABER) plots closely overlapping the AIRS observation in both time and spatial extent. Plots (e–h) show the same for observations at 3.2 UT. The dots in plot (a) and (e) show the SABER location of the measurement, and the colors correspond to those used in plots (b–d) and (f–h).

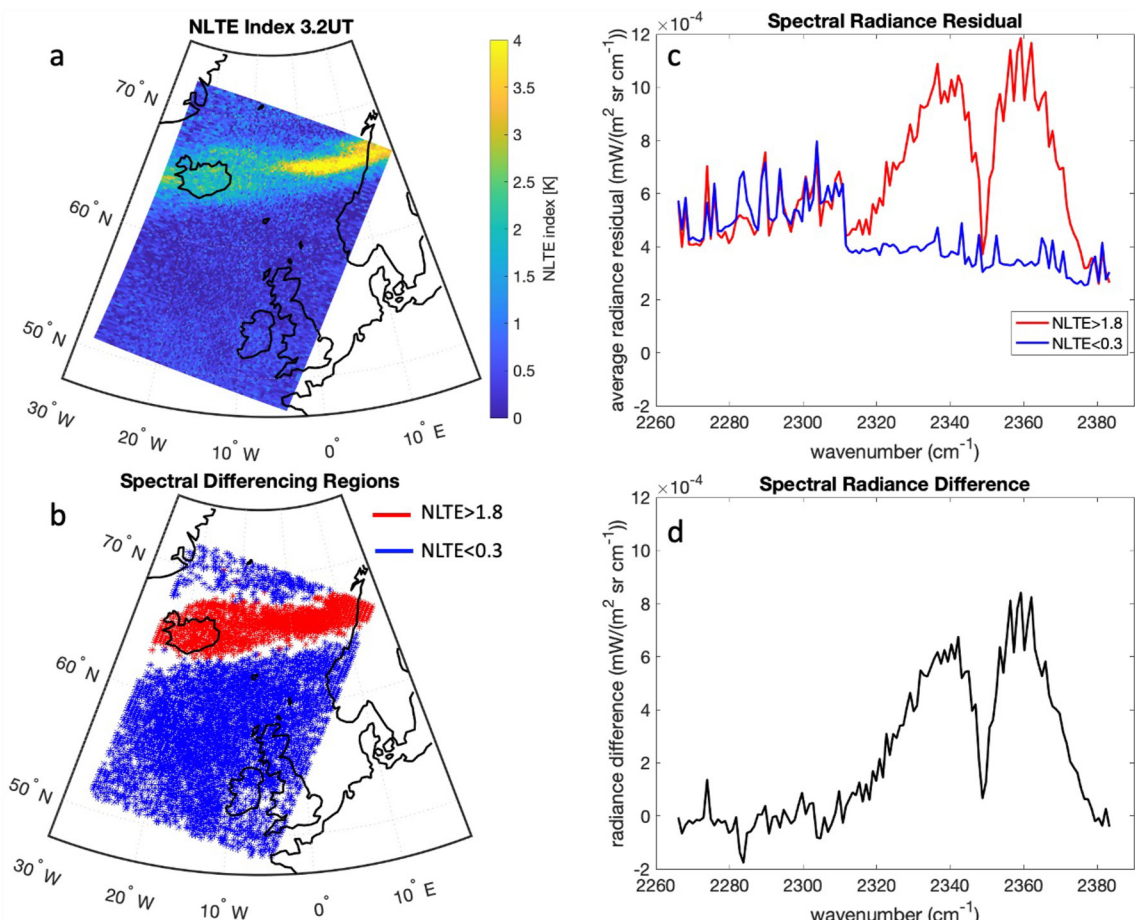


**Figure 4.** Plot a shows the non-local thermodynamic equilibrium (NLTE) index values at 3.2 UT on 14 October 2016. Plot (b) shows the masked NLTE index value regions with values  $<0.3$  in blue, and regions of high NLTE index with values  $>1.8$  in red. Plot (c) shows the average residual spectral radiance values for the high and low NI regions. Plot (d) shows the spectral radiance difference between the high NI and low NI regions.

would otherwise be weak compared to emissions from  $\text{CO}_2$  viewed from the nadir, as is the case with the AIRS measurements. Also, SABER does not have the spectral resolution to differentiate those  $4.26\text{ }\mu\text{m}$  emissions that occur from  $\text{CO}_2$  versus  $\text{NO}^+$ . SABER measurements are shown here to validate that the increased AIRS NLTE index signals overlap regions of auroral emissions. These measurements confirm the presence of aurora and increased  $4.26\text{ }\mu\text{m}$  emission in SABER where AIRS measurements show increased NLTE index calculations.

### 3. Discussion: The $\text{CO}_2$ Auroral Emission

The AIRS instrument can detect emissions in the range of the  $\text{CO}_2$   $4.26\text{ }\mu\text{m}$  ( $2,347\text{ cm}^{-1}$ ) waveband with a spectral resolution of  $\sim 1\text{ cm}^{-1}$ . Given this precision, the emissions outside of the region of NLTE index enhancement due to aurora can be subtracted from the region of enhanced NLTE emission to retrieve a spectral differencing at each wavenumber measured by AIRS, resulting in an emission spectrum associated with auroral emissions. Figure 4 shows an example of this process. Figure 4a shows the NLTE index granule to be used, in this case the event on 14 October at 3.2 UT. Figure 4b shows the regions of low NI with values  $< 0.3$  in blue, and regions of high NLTE index with values  $> 1.8$  in red. In order to remove background emission signal and be left with perturbations solely due to the auroral emission, a fourth order polynomial was fit along each zonal direction of the granule for each emission channel, and the resulting fit was subtracted. It is noted that this was applied to a granule with no small-scale temperature fluctuations (e.g., gravity waves) that would cause significant variations in  $\text{CO}_2$  emission intensity over the area of the granule. Since this subtraction results in the auroral region itself appearing as a perturbation, the absolute value of the residual signal was used for each channel to compare regions of high and low NI. The average of the absolute value residual radiances in the low NLTE index region

is subtracted from the average of the absolute value residual radiances in the high NLTE index region for each observed frequency from 2,266 to 2,383  $\text{cm}^{-1}$ . Due to degradation, some channels were removed based on quality indicators within the Level-1B data files. Channels 1985, 2053, and 2075, or 2295.7, 2334.7, and 2355.4  $\text{cm}^{-1}$  were removed. A total of 118 frequency channels were used in the differencing. The mean of the residual spectral radiance values for NLTE index  $>1.8$  and NLTE index  $<0.3$  are shown in Figure 3c. The resulting mean difference for each channel is shown in Figure 4d.

From the data presented in Figure 4d, the emission is centered at 2,347  $\text{cm}^{-1}$ , and is no longer observed at wave-numbers less than 2,300  $\text{cm}^{-1}$ , which would be expected for the  $\text{CO}_2$  associated auroral emission. The spectral shape closely matches the spectral shape (P,R branch) of the 4.26 micron  $\text{CO}_2$  waveband. This indicates that the AIRS observations are largely from the  $\text{CO}_2$  4.26  $\mu\text{m}$  emission associated with the aurora. Although  $\text{NO}^+$  auroral emissions are also expected, they would occur with a much weaker emission and are likely below the noise threshold of detection of AIRS. The  $\text{CO}_2$  auroral emission has previously been discussed (Kalogerakis et al., 2016; Kumer, 1977; Sharma et al., 2015; Winick et al., 2004) and occurs due to vibrational excitation of  $\text{CO}_2$  due to a collision with a vibrationally excited  $\text{N}_2$  molecule, and subsequent relaxation with emission near 4.26  $\mu\text{m}$ . While the study discussed here specifically focuses on aurora observed during nighttime conditions during strong geomagnetic activity, it is noted that this result would also be expected to occur during any energetic particle precipitation or process that causes a vibrationally excited state of  $\text{N}_2$ . This includes aurora occurring on the dayside, which has not been investigated with the technique presented here.

#### 4. Summary

We have demonstrated that hyperspectral nadir infrared sounders such as AIRS can observe the  $\text{CO}_2$  emissions associated with aurora during nighttime conditions. The AIRS instrument has the spectral resolution to demonstrate that these emissions arise from the  $\text{CO}_2$  emission centered at 4.26  $\mu\text{m}$ . The observations are confirmed to overlap aurora through the use of near-coincident SABER measurements and the SME index data. These are the first nadir satellite observations of confirmed  $\text{CO}_2$  auroral emission. The method presented here highlights a new data set using the derived non-local thermodynamic equilibrium index, which can be used for the study of aurora and associated  $\text{CO}_2$  excitation. This method uses AIRS granules, allowing for a spatial view of the auroral emission, and also providing a map view spanning the auroral oval.

#### Data Availability Statement

All datasets used in this work are publicly available. AIRS calculated NLTE values (Hoffmann, 2023) are available at: <https://datapub.fz-juelich.de/slcs/airs/nlte/>. SABER data are available at: <https://saber.gats-inc.com/data.php>. SME data are available at: <https://supermag.jhuapl.edu/indices>.

#### Acknowledgments

KB acknowledges support from NASA 80NSSC21K0002. MM and LH acknowledge support from the NASA Helio-physics TIMED Project that supports the SABER Instrument Team. We gratefully acknowledge the SuperMAG collaborators for the use of the SME index.

#### References

DeSouza-Machado, S. G., Strow, L. L., Hannon, S. E., Motteler, H. E., Lopez-Puertas, M., Funke, B., & Edwards, D. P. (2007). Fast forward radiative transfer modeling of 4.3 mm nonlocal thermodynamic equilibrium effects for infrared temperature sounders. *Geophysical Research Letters*, 34(1), L01802. <https://doi.org/10.1029/2006GL026684>

Gabrielse, C., Nishimura, T., Chen, M., Hecht, J. H., Kaepller, S. R., Gillies, D. M., et al. (2021). Estimating precipitating energy flux, average energy, and Hall auroral conductance from THEMIS All-Sky-Imagers with focus on mesoscales. *Frontiers in Physiology*, 9, 744298. <https://doi.org/10.3389/fphy.2021.744298>

Gao, H., Xu, J., Chen, G.-M., Zhu, Y., Liu, W., & Wang, C. (2020). Statistical structure of nighttime  $\text{O}_2$  aurora from SABER and its dependence on geomagnetic and solar activities in winter. *Journal of Geophysical Research: Space Physics*, 125(12), e2020JA028302. <https://doi.org/10.1029/2020JA028302>

Gjerloev, J. W. (2012). The SuperMAG data processing technique. *Journal of Geophysical Research*, 117(A9), A09213. <https://doi.org/10.1029/2012JA017683>

Hecht, J. H., Christensen, A. B., Strickland, D. J., & Meier, R. R. (1989). Deducing composition and incident electron spectra from ground-based auroral optical measurements: Variations in oxygen density. *Journal of Geophysical Research*, 94(A10), 13553–13563. <https://doi.org/10.1029/JA094iA10p13553>

Hecht, J. H., Strickland, D. J., & Conde, M. G. (2006). The application of ground-based optical techniques for inferring electron energy deposition and composition change during auroral precipitation events. *Journal of Atmospheric and Solar-Terrestrial Physics*, 68(13), 1502–1519. <https://doi.org/10.1016/j.jastp.2005.06.022>

Hoffmann, L. (2023). AIRS/Aqua observations of non-LTE emissions. *Jülich DATA*, V1. <https://doi.org/10.26165/JUELICH-DATA/PH14EE>

Hoffmann, L., & Alexander, M. J. (2009). Retrieval of stratospheric temperatures from Atmospheric Infrared Sounder radiance measurements for gravity wave studies. *Journal of Geophysical Research*, 114(D7), D07105. <https://doi.org/10.1029/2008JD011241>

Hoffmann, L., Alexander, M. J., Clerbaus, C., Grimsdell, A. W., Meyer, C. I., Rossler, T., & Tournier, B. (2014). Intercomparison of stratospheric gravity wave observations with AIRS and IASI. *Atmospheric Measurement Techniques*, 7(12), 4517–4537. <https://doi.org/10.5194/amt-7-4517-2014>

Hoffmann, L., Xue, X., & Alexander, M. J. (2013). A global view of stratospheric gravity wave hotspots located with Atmospheric Infrared Sounder observations. *Journal of Geophysical Research: Atmospheres*, 118(2), 416–434. <https://doi.org/10.1029/2012JD018658>

Kalogerakis, K. S., Matsiev, D., Sharma, R. D., & Wintersteiner, P. P. (2016). Resolving the mesospheric nighttime 4.3  $\mu\text{m}$  emission puzzle: Laboratory demonstration of new mechanism for OH(v) relaxation. *Geophysical Research Letters*, 43(17), 8835–8843. <https://doi.org/10.1002/2016GL069645>

Kumer, J. B. (1977). Theory of the  $\text{CO}_2$  4.3-micrometer aurora and related phenomena. *Journal of Geophysical Research*, 82(16), 2203–2209. <https://doi.org/10.1029/ja082i016p02203>

Laundal, K. M., & Richmond, A. D. (2016). Magnetic coordinate systems. *Space Science Reviews*, 206(1–4), 27–59. <https://doi.org/10.1007/s11214-016-0275-y>

Li, J., Matsuo, T., & Kilcommons, L. M. (2022). Assimilative mapping of auroral electron energy flux using SSUSI Lyman-Birge-Hopfield (LBH) emissions. *Journal of Geophysical Research: Space Physics*, 127(3), e2021JA029739. <https://doi.org/10.1029/2021JA029739>

Li, Z., Menzel, W. P., Jung, J., Lim, A., Li, J., Matricardi, M., et al. (2020). Improving the understanding of CrIS full spectral resolution nonlocal thermodynamic equilibrium radiances using spectral correlation. *Journal of Geophysical Research: Atmospheres*, 125(16), e2020JD032710. <https://doi.org/10.1029/2020JD032710>

López-Puertas, M., Funke, B., Gil-López, S., von Clarmann, T., Stiller, G. P., Höpfner, M., et al. (2005). Observation of  $\text{NO}_x$  enhancement and ozone depletion in the Northern and Southern Hemispheres after the October–November 2003 solar proton events. *Journal of Geophysical Research*, 110(A9), A09S43. <https://doi.org/10.1029/2005JA011050>

Mertens, C. J., Fernandez, J. R., Xu, X., Evans, D. S., Mlynczak, M. G., & Russell, III, J. M. (2008). A new source of auroral infrared emission observed by TIMED/SABER. *Geophysical Research Letters*, 35(17), L17106. <https://doi.org/10.1029/2008GL034701>

Mertens, C. J., Winick, J. R., Picard, R. H., Evans, D. S., Lopez-Puertas, M., Wintersteiner, P. P., et al. (2008). Influence of solar-geomagnetic disturbances on SABER measurements of 4.3  $\mu\text{m}$  emission and the retrieval of kinetic temperature and carbon dioxide. *Advances in Space Research*, 43(9), 1325–1336. <https://doi.org/10.1016/j.asr.2008.10.029>

Newell, P. T., & Gjerloev, J. W. (2011a). Evaluation of SuperMAG auroral electrojet indices as indicators of substorms and auroral power. *Journal of Geophysical Research*, 116(A12), A12211. <https://doi.org/10.1029/2011JA016779>

Newell, P. T., & Gjerloev, J. W. (2011b). Substorms and magnetosphere characteristic scales inferred from the SuperMAG auroral electrojet indices. *Journal of Geophysical Research*, 116(A12), 12232. <https://doi.org/10.1029/2011JA016936>

O’Neil, R. R., Winick, J. R., Picard, R. H., & Kendra, M. (2007). Auroral  $\text{NO}^+$  4.3  $\mu\text{m}$  emission observed from the midcourse space experiment: Multiplatform observations of 9 February 1997. *Journal of Geophysical Research*, 112(A6), A06327. <https://doi.org/10.1029/2006JA012120>

Randall, C. E., Harvey, V. L., Holt, L. A., Marsh, D. R., Kinnison, D., Funke, B., & Bernath, P. F. (2015). Simulation of energetic particle precipitation effects during the 2003–2004 Arctic winter. *Journal of Geophysical Research: Space Physics*, 120(6), 5035–5048. <https://doi.org/10.1002/2015JA021196>

Randall, C. E., Harvey, V. L., Singleton, C. S., Bailey, S. M., Bernath, P. F., Codrescu, M., et al. (2007). Energetic particle precipitation effects on the Southern Hemisphere stratosphere in 1992–2005. *Journal of Geophysical Research*, 112(D8), D08308. <https://doi.org/10.1029/2006JD007696>

Seaman, C. J., & Miller, S. D. (2013). VIIRS captures aurora motions. *Bulletin of the American Meteorological Society*, 94(10), 1491–1493. <https://doi.org/10.1175/BAMS-D-12-00221.1>

Sharma, R. D., Wintersteiner, P. P., & Kalogerakis, K. S. (2015). A new mechanism for OH vibrational relaxation leading to enhanced  $\text{CO}_2$  emissions in the nocturnal atmosphere. *Geophysical Research Letters*, 42(11), 4639–4647. <https://doi.org/10.1002/2015GL063724>

Sheng, C., Deng, Y., Zhang, S.-R., Nishimura, Y., & Lyons, L. R. (2020). Relative contributions of ion convection and particle precipitation to exciting large-scale traveling atmospheric and ionospheric disturbances. *Journal of Geophysical Research: Space Physics*, 125(2), e2019JA027342. <https://doi.org/10.1029/2019JA027342>

Sotirelis, T., Korth, H., Hsieh, S.-Y., Zhang, Y., Morrison, D., & Paxton, L. (2013). Empirical relationship between electron precipitation and far-ultraviolet auroral emissions from DMSP observations. *Journal of Geophysical Research: Space Physics*, 118(3), 1203–1209. <https://doi.org/10.1002/jgra.50157>

Strickland, D. J., Meier, R. R., Hecht, J. H., & Christensen, A. B. (1989). Deducing composition and incident electron spectra from ground-based auroral optical measurements: Theory and model results. *Journal of Geophysical Research*, 94(13), 13527–13539. <https://doi.org/10.1029/JA094iA10p13527>

Winick, J. R., Mlynczak, M. G., Wintersteiner, P. P., Martin-Torres, F. J., Picard, R. H., Paxton, L. J., et al. (2004). Thermospheric infrared radiance response to the April 2002 geomagnetic storm from SABER infrared and GUVI ultraviolet limb data. *Proceedings of SPIE*, 5235. <https://doi.org/10.1117/12.515982>

Winick, J. R., Picard, R. H., Sharma, R. D., Joseph, R. A., & Wintersteiner, P. P. (1987). Radiative transfer effects on aurora enhanced 4.3 micron emission. *Advances in Space Research*, 7(10), 17–21. [https://doi.org/10.1016/0273-1177\(87\)90070-6](https://doi.org/10.1016/0273-1177(87)90070-6)